

Waveform inversion for attenuation estimation in anisotropic media

Tong Bai¹, Ilya Tsvankin¹, and Xinming Wu²

ABSTRACT

Robust estimation of attenuation coefficients remains a challenging problem, especially for heterogeneous anisotropic media. Here, we apply waveform inversion (WI) to perform attenuation analysis in heterogeneous VTI (transversely isotropic with a vertical symmetry axis) media. A time-domain finite-difference algorithm based on the standard linear solid model simulates nearly constant quality-factor values in a specified frequency band. We employ the adjoint-state method to derive the gradients of the objective function based on the Born approximation. Four parameters describing the attenuation coefficients of P- and SV-waves are updated simultaneously with a quasi-Newton optimization algorithm. To remove the time shifts between the modeled and observed data caused by velocity errors, we apply a local similarity technique. The inversion still requires a sufficiently accurate velocity model to minimize the trade-off between the contributions of velocity and attenuation to amplitudes. The inversion algorithm is tested on homogeneous background models with a Gaussian anomaly in one of the attenuation parameters and on a realistic heterogeneous VTI medium.

INTRODUCTION

Viscoelasticity is a ubiquitous property of the subsurface, which produces energy dissipation and velocity dispersion during wave propagation. Attenuation coefficients can be utilized to obtain important information about reservoir rocks such as the fluid type, saturation, and mechanical properties of the rock matrix (Johnston et al., 1979; Tiwari and McMechan, 2007). Besides, correcting for attenuation helps improve the results of inversion and imaging

in viscoelastic/viscoacoustic media (e.g., Causse et al., 1999; Zhu et al., 2014; Xue et al., 2016).

Formations that exhibit velocity anisotropy are often characterized by even stronger attenuation anisotropy (Zhu et al., 2006; Best et al., 2007; Chichinina et al., 2009). Laboratory experiments have shown that attenuation anisotropy may help estimate the orientation and properties of aligned fractures and the presence of organic laminae inside the rocks (Chichinina et al., 2006; Best et al., 2007; Clark et al., 2009; Ekanem et al., 2013).

Attenuation coefficients can be estimated from the reduction in the dominant frequency of the signal, which is the main idea behind the centroid frequency shift method (CFSM) and the peak frequency shift method (PFSM) (Quan and Harris, 1997). However, both methods are valid only for certain wavelet types characterized by a Gaussian amplitude spectrum (de Castro Nunes et al., 2011). The spectral-ratio method (SRM) (e.g., Sams and Goldberg, 1990) estimates the quality factor Q in the frequency domain from the slope of the amplitude ratio of two arrivals. Although the performance of SRM depends on the chosen frequency band and on the clipping function applied at the edges of the bandwidth, it can separate attenuation from geometric spreading, reflection/transmission coefficients and other frequency-independent amplitude factors. Also, SRM is generally more stable than other conventional methods (e.g., CFSM or PFSM) for attenuation estimation (de Castro Nunes et al., 2011).

For anisotropic media, SRM-based layer-stripping schemes for P- and S-wave attenuation analysis are proposed by Behura and Tsvankin (2009) and Shekar and Tsvankin (2011). However, all conventional methods are generally limited to structurally simple subsurface models and may give erroneous results in the presence of interference (Hackert and Parra, 2004; Reine et al., 2012).

Waveform inversion (WI) can potentially provide more robust attenuation estimation for realistic subsurface structures. Originally introduced by Tarantola (1984), WI has been widely used for building high-resolution velocity models, with the influence of attenuation often neglected for simplicity. However, applying purely acoustic WI to viscoacoustic data may distort the recovered velocity

Manuscript received by the Editor 18 November 2016; revised manuscript received 17 March 2017; published online 19 June 2017.

¹Center for Wave Phenomena, Colorado School of Mines, Golden, Colorado, USA. E-mail: tbai@mines.edu; ilya@mines.edu.

²Colorado School of Mines, Department of Geophysics, Golden, Colorado, USA and University of Texas at Austin, Bureau of Economic Geology, Austin, Texas, USA. E-mail: xinming.wu@beg.utexas.edu.

© 2017 Society of Exploration Geophysicists. All rights reserved.

profile (e.g., Kurzmann et al., 2013). Significantly improved inversion results can be achieved by including even smoothly varying Q -models in the simulation. In another example discussed by Causse et al. (1999), a viscoacoustic WI algorithm with preconditioning helps compensate for attenuation-induced phase and amplitude distortions, and consequently yields a more accurate velocity field.

Recent progress in multiparameter waveform inversion makes it possible to extend WI to anisotropic and/or attenuative models. Al-khalifah and Plessix (2014) present perturbation-based radiation patterns to analyze parameter trade-offs in WI for acoustic VTI media. Kamath and Tsvankin (2016) obtain radiation patterns for elastic VTI media and develop an elastic WI algorithm to resolve four Thomsen parameters simultaneously from P- and SV-wave data. To analyze the trade-offs in multiparameter viscoelastic WI for isotropic media, Brossier (2011) conducts synthetic transmission experiments and observes that while attenuation has little impact on velocity estimation, velocity and density can leave a strong imprint on the attenuation coefficients. Therefore, attenuation can be estimated using a hierarchical approach, in which the velocity parameters are recovered prior to attenuation analysis (Kamei and Pratt, 2008; Prieux et al., 2013). The inverted attenuation coefficients, however, usually have a lower resolution than their velocity counterparts (Denli et al., 2013; Barnes et al., 2014). J. Bai and Yingst (2013) apply multiscale WI to estimate the attenuation coefficients for a viscoacoustic version of the Marmousi model. Using the actual velocity field, they obtain an isotropic Q -image with acceptable resolution, which somewhat deteriorates at depth.

By incorporating the generalized standard linear solid model, T. Bai and Tsvankin (2016) devise a time-domain finite-difference algorithm to simulate nearly constant values of the components of the anisotropic quality-factor matrix \mathbf{Q} within a specific frequency band. Numerical examples for 2D models with VTI symmetry for both velocity and attenuation demonstrate that this method produces accurate wavefields even for complicated subsurface structures.

In this paper, we employ the modeling methodology of Bai and Tsvankin (2016) to perform WI for viscoelastic VTI media. First, we briefly discuss the time-domain viscoelastic modeling algorithm designed to produce frequency-independent Q_{ij} -values. Next, the gradients of the WI objective function with respect to the TI attenuation parameters are derived by applying the adjoint-state method. Assuming the velocity field to be known, we invert just for certain combinations of the Thomsen-style attenuation parameters A_{P0} , A_{S0} , ϵ_Q , and δ_Q . We also describe application of a local-similarity technique to reduce the sensitivity of inversion results to velocity errors. The algorithm is tested on transmission data from models with Gaussian anomalies in the attenuation parameters and reflection data simulated for a section of the modified BP TI model.

METHODOLOGY

Forward modeling for viscoelastic VTI media

Viscoelastic wave propagation can be simulated in a relatively straightforward way in the frequency domain by making velocities or stiffness coefficients complex (e.g., Operto et al., 2007; Shekar and Tsvankin, 2014). However, frequency-domain full-waveform modeling methods (e.g., finite-differences) are hampered by excessive memory requirements (Virieux et al., 2009). Aside from their advantage in large-scale applications, time-domain simulations are

generally more robust for complex (e.g., elastic and anisotropic) models and facilitate selection of specific arrivals for attenuation analysis (Virieux et al., 2009; Kurzmann et al., 2013).

To generate constant Q -values for the seismic frequency band in time-domain modeling, it is common to employ superposition of several rheological bodies, each providing one relaxation mechanism (Emmerich and Korn, 1987; Carcione, 1993; Blanch et al., 1995; Bohlen, 2002). In most seismic applications, two to three relaxation mechanisms are sufficient for a nearly constant- Q simulation (Emmerich and Korn, 1987; Bohlen, 2002; Bai and Tsvankin, 2016). Zhu et al. (2013) observe that even one mechanism with properly chosen parameters can produce reasonably accurate results within the frequency band typical for surface seismic surveys.

Here, primarily for purposes of computational efficiency, we employ a single relaxation mechanism. The expressions for the corresponding stress relaxation time and attenuation parameters τ_{ij} can be found in Appendix A. As discussed by Bai and Tsvankin (2016), anisotropic attenuation can be described by the following relaxation function (shown here with one relaxation mechanism):

$$\Psi_{ijkl}(t) = C_{ijkl}^R(1 + \tau_{ijkl}e^{-t/\tau^\sigma})H(t), \quad (1)$$

where $C_{ijkl}^R = \Psi_{ijkl}(t \rightarrow \infty)$ is called the “relaxed stiffness,” which corresponds to the low-frequency limit ($\omega = 0$), τ^σ denotes the stress relaxation time determined by the reference frequency (equation A-1), the tensor $\tau_{ijkl} \approx 2/Q_{ijkl}$ (see equation A-2), which quantifies the magnitude of attenuation in anisotropic media, is commonly used in time-domain viscoacoustic/viscoelastic modeling, and $H(t)$ is the Heaviside function. The relaxation function at zero time yields the “unrelaxed stiffness”:

$$C_{ijkl}^U \equiv \Psi_{ijkl}(t = 0) = C_{ijkl}^R(1 + \tau_{ijkl}). \quad (2)$$

The stiffness difference $\Delta C_{ijkl} = C_{ijkl}^U - C_{ijkl}^R$ (equation A-3) is proportional to τ_{ijkl} and, therefore, reflects the magnitude of attenuation.

The attenuation of P- and SV-waves in VTI media can be described by four Thomsen-style attenuation parameters, A_{P0} , A_{S0} , ϵ_Q , and δ_Q (Zhu and Tsvankin, 2006). The parameters A_{P0} and A_{S0} denote the P- and S-wave attenuation coefficients in the vertical (symmetry-axis) direction (equations C-1 and C-2), the parameter ϵ_Q quantifies the fractional difference between the horizontal and vertical P-wave attenuation coefficients, and δ_Q controls the curvature of the P-wave attenuation coefficient at the symmetry axis (equations C-3 and C-4). Combined with the unrelaxed stiffness coefficients C_{ijkl}^U (used as the reference elastic parameters), these attenuation parameters can be converted into the quality-factor elements Q_{ijkl} (or ΔC_{ijkl} , as in equation A-3).

The viscoelastic stress-strain relationship (an extension of Hooke’s law to attenuative models) can be expressed as

$$\sigma_{ij} = C_{ijkl}^U \epsilon_{kl} + \Delta C_{ijkl} r_{kl}, \quad (3)$$

where r_{kl} are the memory variables, which satisfy the following partial differential equations (Bai and Tsvankin, 2016):

$$\frac{\partial r_{kl}}{\partial t} = -\frac{1}{\tau^\sigma}(r_{kl} + \epsilon_{kl}). \quad (4)$$

Viscoelastic waveform inversion

WI utilizes the entire waveforms of certain arrivals (e.g., diving waves and/or reflections) to iteratively update the model parameters. The degree of data fitting is usually evaluated with an ℓ_2 -norm objective function (e.g., Tarantola, 1988; Tromp et al., 2005):

$$F(\mathbf{m}) = \frac{1}{2} \sum_{r=1}^N \|\mathbf{u}(x_r, t, \mathbf{m}) - \mathbf{d}(x_r, t)\|^2, \quad (5)$$

where $\mathbf{u}(x_r, t, \mathbf{m})$ denotes the data computed for the trial model \mathbf{m} , $\mathbf{d}(x_r, t)$ is the observed data, r is the receiver index, and t is the time; summation over shots is implied. Instead of calculating the Fréchet derivatives, which can be prohibitively expensive, the gradient of the objective function is typically computed with the adjoint-state method (Tarantola, 1988; Fichtner, 2005; Tromp et al., 2005). Then just two simulations of wave propagation (forward and adjoint) are required to update the model at each iteration.

In viscoelastic media, the adjoint wavefield is “propagated backward in time, with numerically stable negative attenuation” (Tarantola, 1988). Tromp et al. (2005) and Fichtner and Van Driel (2014) present the adjoint equations for general anisotropic attenuative media, but implement them only for isotropic attenuation. Following Tarantola (1988) and applying the Born approximation, the gradients for the viscoelastic parameters ΔC_{ijkl} (equation A-3) can be expressed as the cross-correlation of the memory variables from the forward simulation with the adjoint strain field (Appendix B):

$$\delta \Delta C_{ijkl} = - \sum_{\text{sources}} \int_0^T \frac{\partial u_i^\dagger}{\partial x_j} r_{kl} dt, \quad (6)$$

where \mathbf{u}^\dagger denotes the adjoint displacement field.

In waveform inversion, it is convenient to choose parameters that have the same units and similar magnitude (e.g., Plessix and Cao, 2011; Kamath and Tsvankin, 2016). Also it is common to use the inverse quality factor Q^{-1} (i.e., the attenuation coefficient) in WI algorithms for attenuative media (Liao and McMechan, 1995; Bai and Yingst, 2013). Therefore, here we describe TI attenuation by the P- and S-wave symmetry-direction attenuation coefficients A_{P0} and A_{S0} (equations C-1 and C-2) and two more parameters, A_{Ph} and A_{Pn} , which quantify the magnitude of attenuation anisotropy. The P-wave horizontal attenuation coefficient A_{Ph} is given by:

$$A_{Ph} = (1 + \epsilon_Q) A_{P0} \approx \frac{1}{2Q_{11}}. \quad (7)$$

To account for the attenuation-anisotropy coefficient δ_Q , we define the parameter A_{Pn} :

$$A_{Pn} = (1 + \delta_Q) A_{P0}, \quad (8)$$

which governs the angular variation of the P-wave attenuation near the symmetry axis and has a form similar to the linearized normal-moveout (NMO) velocity for a horizontal VTI layer. As described in Appendix C, the gradients for the stiffness differences ΔC_{ijkl} can be converted into those for the attenuation coefficients A_{P0} , A_{S0} , A_{Ph} , and A_{Pn} by applying the chain rule (equations C-6–C-8).

To reduce the ambiguity of the inverse problem, we assume the velocity parameters (C_{ijkl}^V) and density to be known. This prevents cycle-skipping in the inversion because the influence of attenuation-

induced dispersion in the seismic frequency band is typically small (Zhu and Tsvankin, 2006; Kurzmann et al., 2013). Hence, the WI algorithm can operate with relatively high frequencies to increase the sensitivity of the wavefield to attenuation. As shown below, the influence of moderate velocity errors can be mitigated by applying the local similarity technique. Model updating is performed with the help of the limited-memory Broyden-Fletcher-Goldfarb-Shanno (L-BFGS) algorithm, which scales the gradients by an approximate inverse Hessian matrix.

SYNTHETIC EXAMPLES

Transmission tests

Here we conduct a series of transmission experiments for Gaussian anomalies in the Thomsen-style attenuation parameters embedded in a homogeneous VTI background. The wavefield is excited by displacement sources with the orientation specified in the figure captions. The velocity parameters V_{P0} , V_{S0} , ϵ , and δ and the density are constant and kept at the actual values during the inversion. The reference frequency, which determines the stress relaxation time (equation A-1) needed in the viscoelastic wave equation (equation A-8), is set equal to the central frequency of the wavelet (30 Hz in all transmission experiments). Starting from the homogeneous background model, we conduct simultaneous inversion for the attenuation parameters A_{P0} , A_{S0} , A_{Ph} , and A_{Pn} using the gradients of the objective function obtained in equations C-5–C-8.

First, we introduce a Gaussian anomaly in A_{P0} and place horizontal arrays of sources and receivers above and below the anomaly (Figure 1). Because the parameters ϵ_Q and δ_Q are constant, there are anomalies in A_{Ph} and A_{Pn} as well (equations 7–8). Although much of the A_{P0} -anomaly is well recovered (Figure 2a), its shape is somewhat distorted. The update in the shear-wave coefficient A_{S0} is negligible (Figure 2b), as expected, because P-wave attenuation in Thomsen-style notation is practically independent of A_{S0} (Zhu and Tsvankin, 2006; Tsvankin and Grechka, 2011; Hao and Alkhailah, 2016). The P-wave horizontal attenuation coefficient A_{Ph} is only partially recovered, with the underestimated magnitude of the

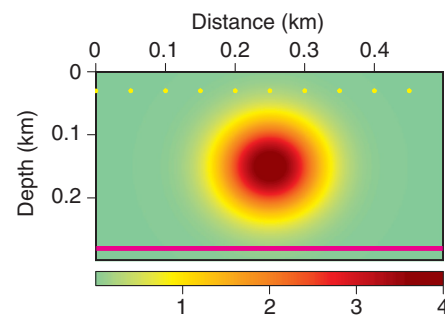


Figure 1. Gaussian anomaly in the parameter A_{P0} embedded in a homogeneous VTI medium. The plot shows the fractional difference between A_{P0} and its background value [defined as $(A_{P0}^{\text{actual}} - A_{P0}^{\text{background}})/A_{P0}^{\text{background}}$], 0.005 ($Q_{P0} = 100$); at the center of the anomaly, $A_{P0} = 0.025$ ($Q_{P0} = 20$). The other pertinent parameters are constant: $A_{S0} = 0.005$, $\epsilon_Q = -0.2$, $\delta_Q = -0.4$, $V_{P0} = 4000$ m/s, $V_{S0} = 2000$ m/s, $\epsilon = 0.15$, $\delta = 0.1$, and $\rho = 2.0$ g/cm³. The yellow dots denote the vertical displacement sources, which excite a Ricker wavelet with a central frequency of 30 Hz. The magenta line marks the receivers placed at each grid point.

reconstructed anomaly (Figure 2c). The errors in A_{Ph} are likely due to the limited ray coverage near the horizontal direction. Note that the difference between ϵ_Q and δ_Q is well constrained because it determines the magnitude of attenuation anisotropy for SV-waves (Zhu and Tsvankin, 2006), which significantly influences the multi-component data for this model. According to equations 7 and 8, the ratio A_{Pn}/A_{Ph} depends on $\epsilon_Q - \delta_Q$ and, therefore, the insufficient update in A_{Ph} produces an underestimated value of A_{Pn} (Figure 2d).

Next, we introduce a Gaussian anomaly in the shear-wave attenuation coefficient A_{S0} (Figure 3). In this test, the inversion algorithm updates only A_{S0} , which indicates the absence of parameter trade-offs (Figure 4b). The peak of the reconstructed anomaly ($A_{S0} = 0.022$ or $Q_{S0} = 23$) is close to the actual value ($A_{S0} = 0.025$ or $Q_{S0} = 20$), although the shape is slightly distorted. Figure 5 demonstrates that the data residuals are substantially reduced after the inversion.

Similarly, in a “crosswell” survey for a model with a negative Gaussian anomaly in ϵ_Q (Figure 6), the algorithm accurately esti-

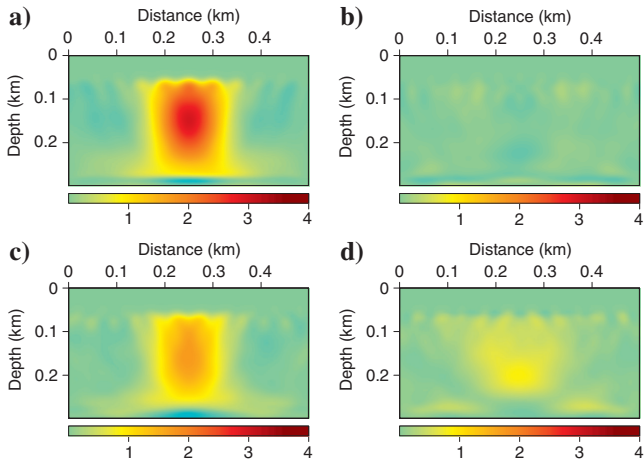


Figure 2. Fractional differences between the inverted and initial parameters for the model from Figure 1: (a) A_{P0} , (b) A_{S0} , (c) A_{Ph} , and (d) A_{Pn} . The peak value of the recovered anomaly in A_{P0} is 0.02 (about 80% of the actual maximum). The parameters A_{Ph} and A_{Pn} are underestimated (the updated maximum values are 0.011 and 0.006, whereas the actual peak magnitudes are 0.02 and 0.015, respectively).

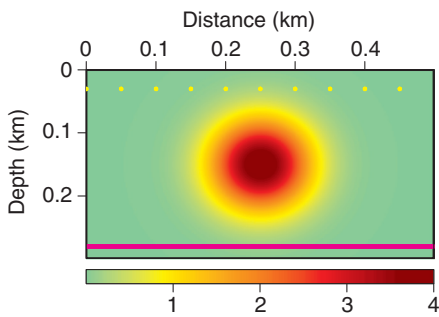


Figure 3. Gaussian anomaly in the parameter A_{S0} embedded in a homogeneous VTI medium. The plot shows the fractional difference between A_{S0} and its background value, 0.005 ($Q_{S0} \approx 100$); at the center of the anomaly, $A_{S0} = 0.025$ ($Q_{S0} \approx 20$). The other parameters are constant: $A_{P0} = 0.005$, $\epsilon_Q = -0.2$, $\delta_Q = -0.4$, $V_{P0} = 4000$ m/s, $V_{S0} = 2000$ m/s, $\epsilon = 0.15$, $\delta = 0.1$, and $\rho = 2.0$ g/cm³. The yellow dots denote the horizontal displacement sources and the magenta line marks the receivers placed at each grid point.

mates the only perturbed parameter, $A_{Ph} = A_{P0}(1 + \epsilon_Q)$. Both the shape and peak magnitude of the anomaly ($\epsilon_Q = -0.72$, about 90% of the actual minimum) are well resolved.

Test for surface data

Next, we test the algorithm on surface data simulated for a modified section of the TI model generated by BP, which has been widely used in testing of anisotropic velocity-analysis techniques (Figure 8). The velocity parameters and density have a spatial distribution similar to that of the attenuation parameters and are not shown here; the tilt of the symmetry axis was set to zero to make the model VTI. At a depth of 0.3 km, we place 30 evenly spaced displacement sources (tilted by 45° from the vertical) which excite a Ricker wavelet with a central frequency of 20 Hz; the receivers

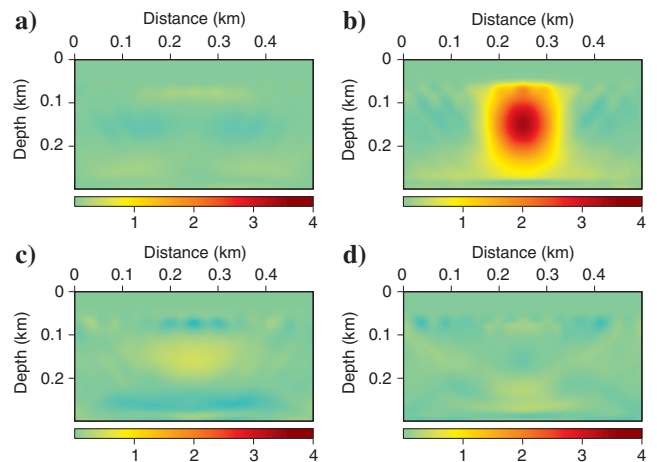


Figure 4. Fractional differences between the inverted and initial parameters for the model from Figure 3: (a) A_{P0} , (b) A_{S0} , (c) A_{Ph} , and (d) A_{Pn} . The peak value of the recovered anomaly in A_{S0} is 0.022 (about 88% of the actual maximum).

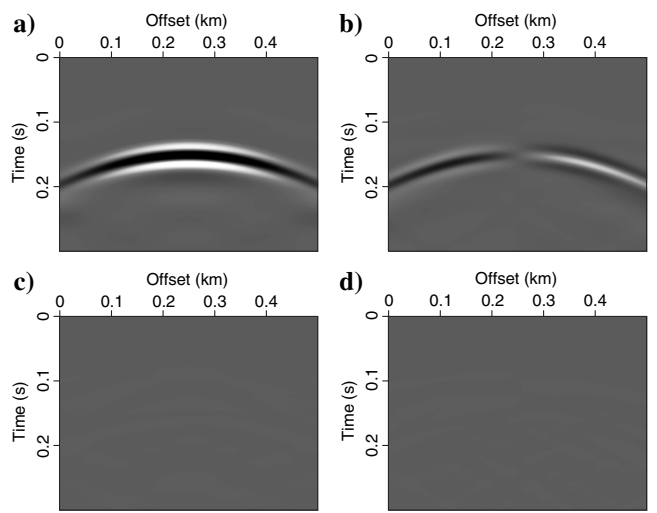


Figure 5. Difference between the observed and simulated data for the model in Figure 3; the source is located at $x = 0.25$ km. The residuals for the initial model: (a) z-component; (b) x-component. The residuals for the inverted model after 17 iterations: (c) z-component; (d) x-component.

are located at each grid point (Figure 8a). Triangle filtering with a smoothing radius of 25 samples in both the vertical and horizontal directions is applied to obtain smooth initial models of the attenuation parameters suitable for the L-BFGS algorithm (Figure 9).

After 18 iterations, the objective function is significantly reduced (Figure 10), and the long-wavelength spatial distribution of the at-

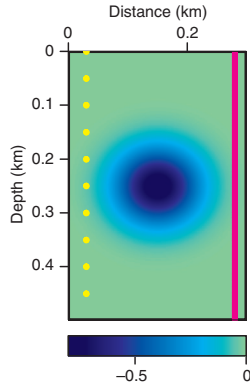


Figure 6. Negative Gaussian anomaly in the parameter ϵ_Q embedded in a homogeneous VTI medium. The plot shows the fractional difference between the parameter $A_{Ph} = A_{P0}(1 + \epsilon_Q)$ and its background value, 0.025 (the background $\epsilon_Q = 0$); at the center of the anomaly, $A_{Ph} = 0.005$ ($\epsilon_Q = -0.8$). The other parameters are constant: $A_{P0} = 0.025$, $A_{S0} = 0.025$, $\delta_Q = 0.4$, $V_{P0} = 4000$ m/s, $V_{S0} = 2000$ m/s, $\epsilon = 0.15$, $\delta = 0.1$, and $\rho = 2.0$ g/cm³. The yellow dots denote the horizontal displacement sources and the magenta line marks the receivers placed at each grid point.

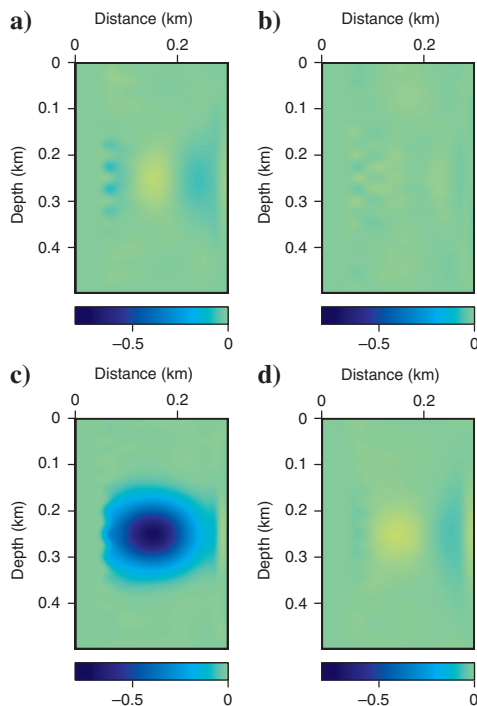


Figure 7. Fractional differences between the inverted and initial parameters for the model from Figure 6: (a) A_{P0} , (b) A_{S0} , (c) A_{Ph} , and (d) A_{Pn} . The peak value of the recovered anomaly in ϵ_Q is -0.72 (about 90% of the actual minimum).

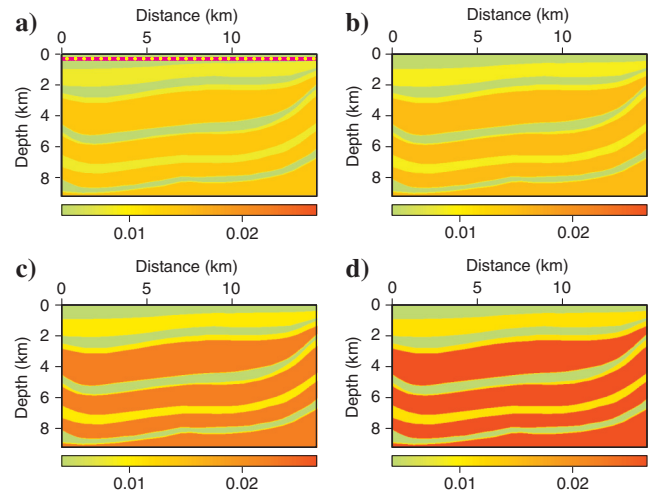


Figure 8. Attenuation parameters for a modified section of the BP TI model: (a) A_{P0} , (b) A_{S0} , (c) A_{Ph} , and (d) A_{Pn} . The symmetry axis is vertical. The model size is 15000 m × 9250 m, with grid spacing $\Delta x = \Delta z = 25$ m. The yellow dots on plot (a) denote the displacement sources, and the magenta line marks the receivers placed at each grid point.

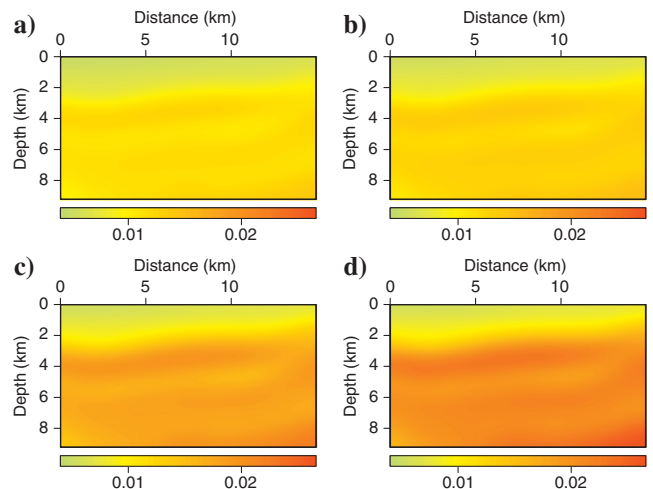


Figure 9. Smoothed actual parameters used as the initial model: (a) A_{P0} , (b) A_{S0} , (c) A_{Ph} , and (d) A_{Pn} .

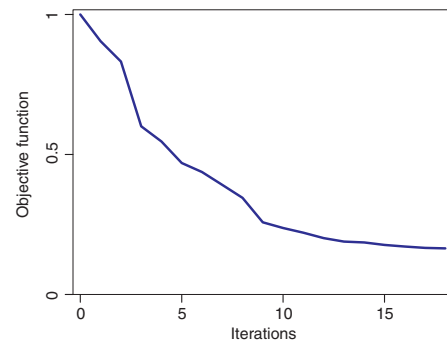


Figure 10. Change of the objective function with iterations for the reflection experiment in Figure 8.

tenuation parameters A_{P0} and A_{S0} (Figure 11) is recovered even in the deeper part of the section (Figure 11a and 11b). The profiles in Figure 12 illustrate the accuracy of the parameter updates obtained by WI. The estimated A_{P0} and A_{S0} generally follow the trends of the actual profiles, and A_{Ph} is accurately estimated down to 5 km. In contrast, the reconstruction of A_{Pn} is less accurate, likely due to the smaller wavefield sensitivity to the parameter δ_Q .

Mitigation of velocity errors

The numerical experiments above are carried out under the assumption that all velocity parameters are known, which is not realistic in practice. To evaluate the sensitivity of the algorithm to velocity errors, we use the model in Figure 8 with distorted

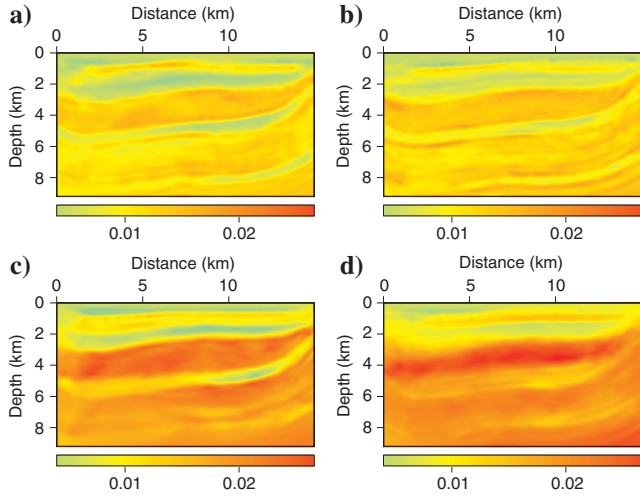


Figure 11. Inverted attenuation parameters: (a) A_{P0} , (b) A_{S0} , (c) A_{Ph} , and (d) A_{Pn} .

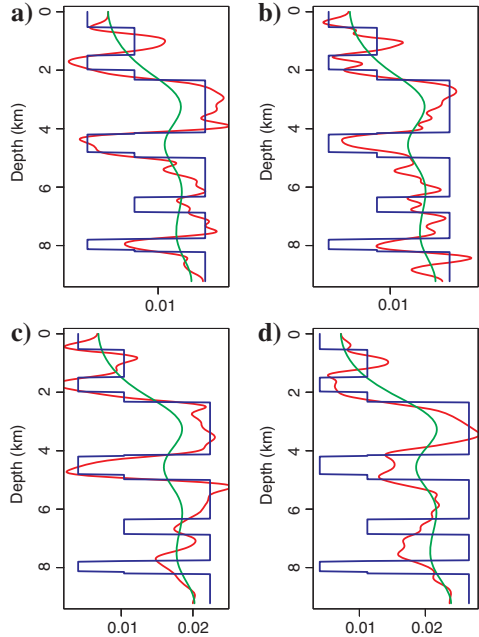


Figure 12. Profiles of the attenuation parameters at $x = 10$ km: (a) A_{P0} , (b) A_{S0} , (c) A_{Ph} , and (d) A_{Pn} . The blue, green, and red lines mark the actual, initial, and inverted values, respectively.

P- and S-wave vertical velocities V_{P0} and V_{S0} (set to 95% of the actual values throughout the section), while ϵ and δ remain exact. As expected, velocity errors produce shifts between the observed and simulated events, leading to distorted adjoint sources (Figure 13) and deterioration in the inversion results (Figure 14).

To reduce the influence of velocity errors on the inversion, we estimate the local similarity map (Fomel, 2009; Fomel and Jin, 2009) from the recorded and modeled arrivals and pick the trend with the global maximum of the similarity values using ray tracing

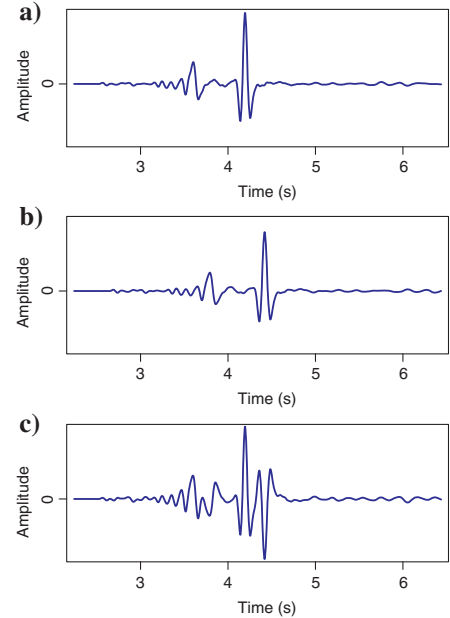


Figure 13. Vertical displacement for the model in Figure 8; the source is located at $x = 0$ and receiver at $x = 7.5$ km. (a) The observed data, (b) the data simulated for the first iteration with an inaccurate velocity model (V_{P0} and V_{S0} are set to 95% of the actual values), (c) the difference between traces on plots (a) and (b).

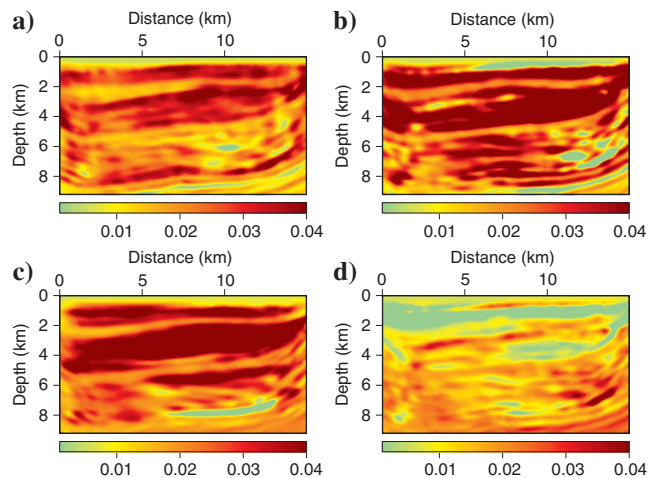


Figure 14. Attenuation parameters estimated with the distorted velocity model: (a) A_{P0} , (b) A_{S0} , (c) A_{Ph} , and (d) A_{Pn} . The upper limit of all parameters (for the L-BFGS algorithm) is set to 0.04, which corresponds to the quality factor close to 12.5.

(Fomel, 2009). This helps calculate the time shifts and then align the corresponding events prior to WI (Figure 15). The original ℓ_2 -norm objective function (equation 5) can be modified as

$$F(\mathbf{m}) = \frac{1}{2} \sum_{r=1}^N \|\mathbf{u}(x_r, t, \mathbf{m}) - \mathbf{S}(x_r, t)\mathbf{d}(x_r, t)\|^2, \quad (9)$$

where $\mathbf{S}(x_r, t)$ is a linear interpolation operator that shifts the recorded events based on the local similarity method. $\mathbf{S}(x_r, t)$ is prac-

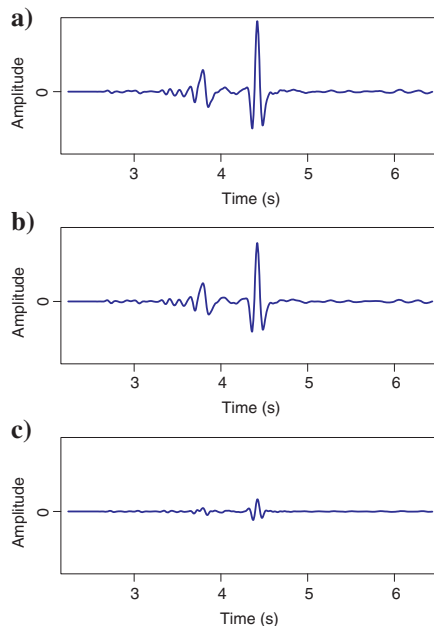


Figure 15. Same as Figure 13, but the observed arrivals on plot (a) are warped (shifted) using the local similarity technique. (b) The data simulated for the first iteration with an inaccurate velocity model (V_{P0} and V_{S0} are set to 95% of the actual values), (c) the difference between the traces on plots (a) and (b).

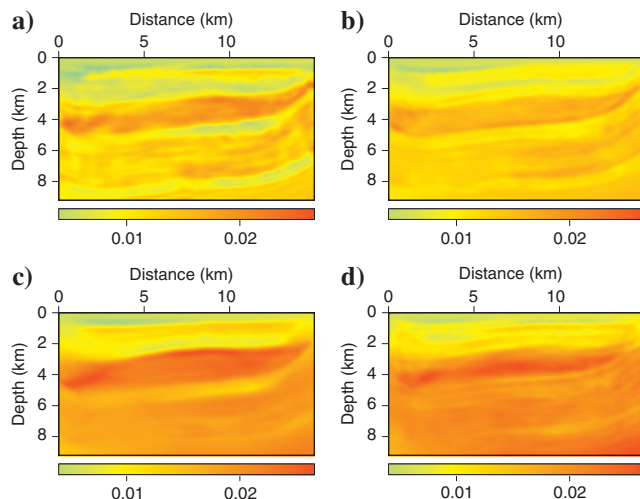


Figure 16. Attenuation parameters estimated with the distorted velocity model after applying the local similarity technique (Figure 15): (a) A_{P0} , (b) A_{S0} , (c) A_{Ph} , and (d) A_{Pn} .

tically independent of the attenuation parameters (\mathbf{m}) when the dispersion is relatively weak. Consequently, the gradient with respect to the attenuation parameter m becomes

$$\frac{\partial F(\mathbf{m})}{\partial m} = \sum_{r=1}^N \left[\frac{\partial \mathbf{u}(x_r, t, \mathbf{m})}{\partial m} \right]^T [\mathbf{u}(x_r, t, \mathbf{m}) - \mathbf{S}(x_r, t)\mathbf{d}(x_r, t)]. \quad (10)$$

The only difference between equation 10 and the gradient for the original data is in the form of the data residual. Expressions similar to equations 9 and 10 can be found in Luo and Hale (2014) who apply dynamic warping to mitigate the influence of velocity errors on least-squares migration.

After the correction, the algorithm generates more accurate adjoint sources and inversion gradients, which improves the parameter-estimation results (compare Figures 16 and 14).

DISCUSSION

The source-receiver configuration in the transmission experiments is designed to better constrain the perturbed attenuation parameters. The anomaly in the P-wave vertical attenuation coefficient A_{P0} was recovered using near-vertical raypaths, whereas crosshole geometry was employed for estimating the coefficient A_{Ph} , which is responsible for the P-wave attenuation near the horizontal isotropy plane. It would be beneficial to investigate the so-called “radiation patterns” (Alkhalifah and Plessix, 2014; Kamath and Tsvankin, 2016) of the attenuation parameters, which could help identify trade-offs for given acquisition geometries and devise a robust multiparameter inversion strategy.

In addition to its influence on kinematics, an inaccurate velocity field also distorts recorded amplitudes through errors in geometric spreading and reflection/transmission coefficients. Compensation for such amplitude errors by our algorithm can cause distortions in the inverted attenuation parameters. The spectral-ratio and centroid-frequency-shift method separate attenuation from other factors by performing attenuation analysis in the frequency domain. A similar approach could be devised to improve the robustness of WI-based attenuation estimation (e.g., Dutta and Schuster, 2016), which is the topic of our ongoing work.

CONCLUSIONS

We presented a time-domain WI methodology for attenuation estimation in transversely isotropic media. The finite-difference modeling algorithm simulates a nearly constant Q -matrix in the seismic frequency band using one relaxation mechanism. By applying the adjoint-state method, we obtained the gradients of the objective function with respect to the viscoelastic parameters ΔC_{ijkl} through the cross-correlations of the memory variables (computed from the forward simulation) with the adjoint strain field. Then the gradients for the VTI attenuation parameters A_{P0} , A_{S0} , A_{Ph} , and A_{Pn} are found using the chain rule.

The inversion algorithm was first tested on homogeneous VTI models with a Gaussian anomaly in one of the Thomsen-style attenuation parameters. A perturbation in A_{P0} (with fixed ϵ_Q and δ_Q) leads to the corresponding anomalies in the parameters A_{Ph} and A_{Pn} . With horizontal arrays of sources and receivers, the algorithm recovers most of the anomaly in A_{P0} , but A_{Ph} and A_{Pn} are only

partially updated. The problem in estimating A_{Ph} and A_{Pn} is likely caused by insufficient illumination near the horizontal direction and trade-offs between the two parameters in the inversion of the multi-component wavefield.

The algorithm was more successful in resolving the anomalies in A_{S0} and ϵ_Q (A_{Ph}). In the absence of measurable cross-talk with the other parameters, WI accurately estimated the shape of both anomalies, despite the slightly distorted peak magnitudes.

Finally, we tested the algorithm on surface data generated for a modified section of the BP TI model. Waveform inversion was able to reconstruct the long-wavelength distribution of the parameters A_{P0} , A_{S0} , and A_{Ph} , and the data misfit was reduced by 70%. We also confirmed the feasibility of mitigating the influence of velocity errors with the local similarity technique.

ACKNOWLEDGMENTS

We are grateful to the members of the A(nisotropy)-Team at CWP for fruitful discussions. The reviews by associate editor Igor Ravve, Faranak Mahmoudian, Tatiana Chichinina, Bharath Shekar and an anonymous referee helped us improve the manuscript. This work was supported by the Consortium Project on Seismic Inverse Methods for Complex Structures at CWP. The reproducible numerical examples in this paper are generated with the Madagascar open-source software package freely available from www.ahay.org.

APPENDIX A

TIME-DOMAIN ANISOTROPIC VISCOELASTIC WAVE EQUATION

Using the standard linear solid model, which includes only one relaxation mechanism, the stress relaxation time τ_σ and the attenuation parameters τ_{ij} (Bai and Tsvankin, 2016) can be approximated as

$$\tau_\sigma \approx \frac{1}{2\pi f_0} \quad (\text{A-1})$$

and

$$\tau_{ij} = \frac{2}{\sqrt{Q_{ij}^2 + 1} - 1} \approx \frac{2}{Q_{ij}}, \quad (\text{A-2})$$

where f_0 denotes the reference frequency, which is often defined as the central frequency of the source wavelet.

The τ_{ij} -parameters, which quantify the magnitude of attenuation in anisotropic media, can be converted into another set of viscoelastic parameters denoted by ΔC_{ij} (Bai and Tsvankin, 2016):

$$\Delta C_{ij} = C_{ij}^U - C_{ij}^R = \frac{C_{ij}^U \tau_{ij}}{1 + \tau_{ij}} \approx \frac{2C_{ij}^U}{2 + Q_{ij}}, \quad (\text{A-3})$$

where C_{ij}^U and C_{ij}^R denote the unrelaxed and relaxed stiffnesses coefficients, respectively. The elements C_{ij}^U , which define the velocity field, are assumed here to be known.

The stress (σ_{ij})-strain (ϵ_{kl}) relationship in anisotropic viscoelastic media can be written as:

$$T_{ij} = \sigma_{ij} - \dot{\Psi}_{ijkl} * \epsilon_{kl}, \quad (\text{A-4})$$

where T_{ij} is the stress tensor and “*” denotes the time-convolution operator.

Parameterizing the relaxation function (equation 1 in the main text) in terms of C_{ij}^U and ΔC_{ij} yields:

$$T_{ij} = \sigma_{ij} - C_{ijkl}^U \epsilon_{kl} + \Delta C_{ijkl} \frac{e^{-t/\tau^\sigma}}{\tau^\sigma} H(t) * \epsilon_{kl}. \quad (\text{A-5})$$

Introducing the memory variables,

$$r_{kl} = -\frac{1}{\tau^\sigma} e^{-t/\tau^\sigma} H(t) * \epsilon_{kl}, \quad (\text{A-6})$$

we rewrite equation A-5 as

$$T_{ij} = \sigma_{ij} - C_{ijkl}^U \epsilon_{kl} - \Delta C_{ijkl} r_{kl}, \quad (\text{A-7})$$

with

$$\dot{r}_{kl} = -\frac{1}{\tau^\sigma} (r_{kl} + \epsilon_{kl}). \quad (\text{A-8})$$

Equations A-7–A-8 and the momentum conservation law constitute the viscoelastic wave equations for VTI media.

APPENDIX B

GRADIENTS FOR VISCOELASTIC PARAMETERS ΔC_{jklm}

In this section, we follow the approach of Charara et al. (2000) to derive the gradients of the objective function with respect to ΔC_{jklm} . Application of the Born approximation to the momentum conservation law and equation A-7 yields:

$$\delta f_i = \rho \delta \ddot{u}_i - \frac{\partial}{\partial x_j} \delta \sigma_{ij} \quad (\text{B-1})$$

and

$$\delta T_{ij} = \delta \sigma_{ij} - C_{ijkl}^U \delta \epsilon_{kl} - \Delta C_{ijkl} \delta r_{kl}, \quad (\text{B-2})$$

where δu_i , $\delta \sigma_{ij}$, $\delta \epsilon_{kl}$, and δr_{kl} are the perturbed wavefield variables, and $\delta \mathbf{f}$ and $\delta \mathbf{T}$ are the virtual force and stress, which are determined by the perturbed model parameters ($\delta \rho$, δC_{ijkl}^U , and $\delta \Delta C_{ijkl}$):

$$\delta f_i = -\ddot{u}_i \delta \rho, \quad (\text{B-3})$$

$$\delta T_{ij} = \epsilon_{kl} \delta C_{ijkl}^U + r_{kl} \delta \Delta C_{ijkl}. \quad (\text{B-4})$$

The solution of the perturbed viscoelastic wave equation can be written as

$$\begin{aligned}\delta u_i &= \int_V dV \int_0^T G_{ij}(\delta f_j) dt - \int_V dV \int_0^T \frac{\partial G_{ij}}{\partial x_k}(\delta T_{jk}) dt \\ &= - \int_V dV \int_0^T G_{ij}(\delta \rho) \ddot{u}_i dt - \int_V dV \int_0^T \frac{\partial G_{ij}}{\partial x_k} dt \\ &\quad \times \left[(\delta C_{jklm}^U) \varepsilon_{lm} + \delta(\Delta C_{jklm}) r_{lm} \right] dt,\end{aligned}\quad (\text{B-5})$$

where G_{ij} denotes the elastic Green's function.

Comparing equation B-5 with

$$\delta \mathbf{u} = \int_V \frac{\partial \mathbf{u}}{\partial \mathbf{m}} \delta \mathbf{m} dV,\quad (\text{B-6})$$

where $\partial \mathbf{u} / \partial \mathbf{m}$ denotes the Fréchet kernel (Tarantola, 1988), we obtain

$$\frac{\partial u_i}{\partial(\Delta C_{jklm})} = - \int_0^T \frac{\partial G_{ij}}{\partial x_k} r_{lm} dt.\quad (\text{B-7})$$

The adjoint of the operator in equation B-6 can be written as

$$\delta m = \sum_{\text{sources}} \int_0^T \left[\frac{\partial u_i}{\partial m} \right]^* \delta u_i dt,\quad (\text{B-8})$$

with the kernels $\partial u_i / \partial \mathbf{m}$ being identical for a linear operator and its transpose (Tarantola, 1988). Then the derivatives of the objective function F with respect to the viscoelastic parameters take the form:

$$\begin{aligned}\frac{\partial F}{\partial(\Delta C_{jklm})} \equiv \delta(\Delta C_{jklm}) &= \sum_{\text{sources}} \int_0^T \left[\frac{\partial u_i}{\partial(\Delta C_{jklm})} \right]^* \delta u_i dt' \\ &= \sum_{\text{sources}} \int_0^T \left[\frac{\partial u_i}{\partial(\Delta C_{jklm})} \right] \delta u_i dt' \\ &= - \sum_{\text{sources}} \int_0^T \int_0^T \frac{\partial G_{ij}}{\partial x_k} r_{lm} \delta u_i dt dt'.\end{aligned}\quad (\text{B-9})$$

By defining the adjoint wavefield as

$$u_j^\dagger = \int_0^T G_{ij} \delta u_i dt,\quad (\text{B-10})$$

we rewrite equation B-9 as

$$\frac{\partial F}{\partial(\Delta C_{jklm})} \equiv \delta(\Delta C_{jklm}) = - \sum_{\text{sources}} \int_0^T \frac{\partial u_j^\dagger}{\partial x_k} r_{lm} dt.\quad (\text{B-11})$$

Therefore, the gradients for the viscoelastic parameters ΔC_{jklm} are the zero-lag cross-correlations of the forward memory variables r_{lm} with the adjoint strain field $\partial u_j^\dagger / \partial x_k$ (Charara et al., 2000).

APPENDIX C GRADIENTS FOR TI ATTENUATION PARAMETERS

The P- and S-wave attenuation coefficients in the symmetry direction can be expressed through the quality-factor matrix Q_{ij} as follows (Zhu and Tsvankin, 2006):

$$A_{P0} \equiv Q_{33} \left(\sqrt{1 + \frac{1}{Q_{33}^2}} - 1 \right) \approx \frac{1}{2Q_{33}}\quad (\text{C-1})$$

and

$$A_{S0} \equiv Q_{55} \left(\sqrt{1 + \frac{1}{Q_{55}^2}} - 1 \right) \approx \frac{1}{2Q_{55}}.\quad (\text{C-2})$$

The influence of attenuation anisotropy on P- and SV-waves is described by the coefficients ε_Q and δ_Q (Zhu and Tsvankin, 2006):

$$\varepsilon_Q \equiv \frac{Q_{33} - Q_{11}}{Q_{11}},\quad (\text{C-3})$$

$$\delta_Q \equiv \frac{1}{2 A_{P0}} \frac{d^2 A_P}{d\theta^2} \Big|_{\theta=0}.\quad (\text{C-4})$$

For inversion purposes, it is convenient to operate with parameters that have similar magnitudes and physical meaning. Here, we employ the horizontal P-wave attenuation coefficient A_{Ph} and a new parameter denoted by A_{Pn} (equations 7 and 8), which absorb the influence of ε_Q and δ_Q , respectively, on the attenuation coefficients.

The gradients for the TI attenuation parameters are then obtained from those for ΔC_{ijkl} (equation B-11) using the chain rule:

$$\frac{\partial F}{\partial A_{Ph}} = \frac{\partial F}{\partial(\Delta C_{11})} \frac{4C_{11}^U}{(1 + 4A_{Ph})^2},\quad (\text{C-5})$$

$$\begin{aligned}\frac{\partial F}{\partial A_{P0}} &= \frac{\partial F}{\partial(\Delta C_{33})} \frac{4C_{33}^U}{(1 + 4A_{P0})^2} \\ &\quad + \frac{\partial F}{\partial(\Delta C_{13})} \frac{4C_{13}^U}{(1 + \tau_{13})^2} \frac{a + b - 1}{b},\end{aligned}\quad (\text{C-6})$$

$$\frac{\partial F}{\partial A_{S0}} = \frac{\partial F}{\partial(\Delta C_{55})} \frac{4C_{55}^U}{(1 + 4A_{S0})^2} + \frac{\partial F}{\partial(\Delta C_{13})} \frac{4C_{13}^U}{(1 + \tau_{13})^2} \frac{(-a)}{b},\quad (\text{C-7})$$

$$\frac{\partial F}{\partial A_{Pn}} = \frac{\partial F}{\partial(\Delta C_{13})} \frac{4C_{13}^U}{(1 + \tau_{13})^2} \frac{1}{b},\quad (\text{C-8})$$

where

$$a \equiv \frac{C_{55}^U}{C_{33}^U} \left(\frac{C_{13}^U + C_{33}^U}{C_{33}^U - C_{55}^U} \right)^2, \quad (\text{C-9})$$

$$b \equiv \frac{2C_{13}^U}{C_{33}^U} \frac{C_{13}^U + C_{55}^U}{C_{33}^U - C_{55}^U}, \quad (\text{C-10})$$

and

$$\tau_{13} = \frac{4}{b} \left[A_{Pn} + (a + b - 1) A_{P0} - a A_{S0} \right]. \quad (\text{C-11})$$

REFERENCES

- Alkhalifah, T., and R.-É. Plessix, 2014, A recipe for practical full-waveform inversion in anisotropic media: An analytical parameter resolution study: *Geophysics*, **79**, no. 3, R91–R101, doi: [10.1190/geo2013-0366.1](https://doi.org/10.1190/geo2013-0366.1).
- Bai, J., and D. Yingst, 2013, *Q* estimation through waveform inversion: 75th Annual International Conference and Exhibition, EAGE, Extended Abstracts, TH-10-01.
- Bai, T., and I. Tsavkin, 2016, Time-domain finite-difference modeling for attenuative anisotropic media: *Geophysics*, **81**, no. 2, C69–C77, doi: [10.1190/geo2015-0424.1](https://doi.org/10.1190/geo2015-0424.1).
- Barnes, C., M. Charara, and P. Williamson, 2014, P & S wave attenuation effects on full-waveform inversion for marine seismic data: 84th Annual International Meeting, SEG, Expanded Abstracts, 949–953.
- Behura, J., and I. Tsavkin, 2009, Estimation of interval anisotropic attenuation from reflection data: *Geophysics*, **74**, no. 6, A69–A74, doi: [10.1190/1.3191733](https://doi.org/10.1190/1.3191733).
- Best, A. I., J. Soothcott, and C. McCann, 2007, A laboratory study of seismic velocity and attenuation anisotropy in near-surface sedimentary rocks: *Geophysical Prospecting*, **55**, 609–625, doi: [10.1111/gpr.2007.55.issue-5](https://doi.org/10.1111/gpr.2007.55.issue-5).
- Blanch, J. O., J. O. Robertson, and W. W. Symes, 1995, Modeling of a constant *Q*: Methodology and algorithm for an efficient and optimally inexpensive viscoelastic technique: *Geophysics*, **60**, 176–184, doi: [10.1190/1.1443744](https://doi.org/10.1190/1.1443744).
- Bohlen, T., 2002, Parallel 3-D viscoelastic finite difference seismic modeling: *Computers & Geosciences*, **28**, 887–899, doi: [10.1016/S0098-3004\(02\)00006-7](https://doi.org/10.1016/S0098-3004(02)00006-7).
- Brossier, R., 2011, Two-dimensional frequency-domain visco-elastic full waveform inversion: Parallel algorithms, optimization and performance: *Computers & Geosciences*, **37**, 444–455, doi: [10.1016/j.cageo.2010.09.013](https://doi.org/10.1016/j.cageo.2010.09.013).
- Carcione, J. M., 1993, Seismic modeling in viscoelastic media: *Geophysics*, **58**, 110–120, doi: [10.1190/1.1443340](https://doi.org/10.1190/1.1443340).
- Causse, E., R. Mittet, and B. Ursin, 1999, Preconditioning of full-waveform inversion in viscoacoustic media: *Geophysics*, **64**, 130–145, doi: [10.1190/1.1444510](https://doi.org/10.1190/1.1444510).
- Charara, M., C. Barnes, and A. Tarantola, 2000, Full waveform inversion of seismic data for a viscoelastic medium, in *Methods and Applications of Inversion*: Springer, 68–81, doi: [10.1007/BFb0010278](https://doi.org/10.1007/BFb0010278).
- Chichinina, T., I. Obolentseva, L. Gik, B. Bobrov, and G. Ronquillo-Jarillo, 2009, Attenuation anisotropy in the linear-slip model: Interpretation of physical modeling data: *Geophysics*, **74**, no. 5, WB165–WB176, doi: [10.1190/1.3173806](https://doi.org/10.1190/1.3173806).
- Chichinina, T., V. Sabinin, and G. Ronquillo-Jarillo, 2006, QVOA analysis: P-wave attenuation anisotropy for fracture characterization: *Geophysics*, **71**, no. 3, C37–C48, doi: [10.1190/1.2194531](https://doi.org/10.1190/1.2194531).
- Clark, R. A., P. M. Benson, A. J. Carter, and C. A. G. Moreno, 2009, Anisotropic P-wave attenuation measured from a multi-azimuth surface seismic reflection survey: *Geophysical Prospecting*, **57**, 835–845, doi: [10.1111/gpr.2009.57.issue-5](https://doi.org/10.1111/gpr.2009.57.issue-5).
- de Castro Nunes, B. I., W. E. De Medeiros, A. F. do Nascimento, and J. A. de Moreira, 2011, Estimating quality factor from surface seismic data: A comparison of current approaches: *Journal of Applied Geophysics*, **75**, 161–170, doi: [10.1016/j.jappgeo.2011.07.003](https://doi.org/10.1016/j.jappgeo.2011.07.003).
- Denli, H., V. Akcelik, A. Kanevsky, D. Trenev, L. White, and M.-D. Lacasse, 2013, Full-wavefield inversion for acoustic wave velocity and attenuation: 83rd Annual International Meeting, SEG, Expanded Abstracts, 980–985.
- Dutta, G., and G. T. Schuster, 2016, Wave-equation *Q* tomography: *Geophysics*, **81**, no. 6, R471–R484, doi: [10.1190/geo2016-0081.1](https://doi.org/10.1190/geo2016-0081.1).
- Ekanem, A., J. Wei, X.-Y. Li, M. Chapman, and I. Main, 2013, P-wave attenuation anisotropy in fractured media: A seismic physical modelling study: *Geophysical Prospecting*, **61**, 420–433, doi: [10.1111/gpr.2013.61.issue-s1](https://doi.org/10.1111/gpr.2013.61.issue-s1).
- Emmerich, H., and M. Korn, 1987, Incorporation of attenuation into time-domain computations of seismic wave fields: *Geophysics*, **52**, 1252–1264, doi: [10.1190/1.1442386](https://doi.org/10.1190/1.1442386).
- Fichtner, A., 2005, The adjoint method in seismology: Theory and application to waveform inversion: AGU Fall Meeting Abstracts, 06.
- Fichtner, A., and M. Van Driel, 2014, Models and Frechet kernels for frequency-(in) dependent *Q*: *Geophysical Journal International*, **198**, 1878–1889, doi: [10.1093/gji/ggu228](https://doi.org/10.1093/gji/ggu228).
- Fomel, S., 2009, Velocity analysis using AB semblance: *Geophysical Prospecting*, **57**, 311–321, doi: [10.1111/gpr.2009.57.issue-3](https://doi.org/10.1111/gpr.2009.57.issue-3).
- Fomel, S., and L. Jin, 2009, Time-lapse image registration using the local similarity attribute: *Geophysics*, **74**, no. 2, A7–A11, doi: [10.1190/1.3054136](https://doi.org/10.1190/1.3054136).
- Hackert, C. L., and J. O. Parra, 2004, Improving *Q* estimates from seismic reflection data using well-log-based localized spectral correction: *Geophysics*, **69**, 1521–1529, doi: [10.1190/1.1836825](https://doi.org/10.1190/1.1836825).
- Hao, Q., and T. Alkhalifah, 2016, An acoustic eikonal equation for attenuating transversely isotropic media with a vertical symmetry axis: *Geophysics*, **82**, no. 1, C9–C20, doi: [10.1190/geo2016-0160.1](https://doi.org/10.1190/geo2016-0160.1).
- Johnston, D. H., M. Toksöz, and A. Timur, 1979, Attenuation of seismic waves in dry and saturated rocks — Part 2: Mechanisms: *Geophysics*, **44**, 691–711, doi: [10.1190/1.1440970](https://doi.org/10.1190/1.1440970).
- Kamath, N., and I. Tsavkin, 2016, Elastic full-waveform inversion for VTI media: Methodology and sensitivity analysis: *Geophysics*, **81**, no. 2, C53–C68, doi: [10.1190/geo2014-0586.1](https://doi.org/10.1190/geo2014-0586.1).
- Kamei, R., and R. G. Pratt, 2008, Waveform tomography strategies for imaging attenuation structure with cross-hole data: 70th Annual International Conference and Exhibition, EAGE, Extended Abstracts, F019.
- Kurzmann, A., A. Przebindowska, D. Köhn, and T. Bohlen, 2013, Acoustic full waveform tomography in the presence of attenuation: A sensitivity analysis: *Geophysical Journal International*, **195**, 985–1000, doi: [10.1093/gji/ggt305](https://doi.org/10.1093/gji/ggt305).
- Liao, O., and G. A. McMechan, 1995, 2.5 D full-wavefield viscoacoustic inversion: *Geophysical Prospecting*, **43**, 1043–1059, doi: [10.1111/gpr.1995.43.issue-8](https://doi.org/10.1111/gpr.1995.43.issue-8).
- Luo, S., and D. Hale, 2014, Least-squares migration in the presence of velocity errors: *Geophysics*, **79**, no. 4, S153–S161, doi: [10.1190/geo2013-0374.1](https://doi.org/10.1190/geo2013-0374.1).
- Operto, S., J. Virieux, P. Amestoy, J.-Y. L'Excellent, L. Giraud, and H. B. H. Ali, 2007, 3D finite-difference frequency-domain modeling of visco-acoustic wave propagation using a massively parallel direct solver: A feasibility study: *Geophysics*, **72**, no. 5, SM195–SM211, doi: [10.1190/1.2759835](https://doi.org/10.1190/1.2759835).
- Plessix, R. -E., and Q. Cao, 2011, A parametrization study for surface seismic full waveform inversion in an acoustic vertical transversely isotropic medium: *Geophysical Journal International*, **185**, 539–556, doi: [10.1111/gji.2011.185.issue-1](https://doi.org/10.1111/gji.2011.185.issue-1).
- Prieux, V., R. Brossier, S. Operto, and J. Virieux, 2013, Multiparameter full waveform inversion of multicomponent ocean-bottom-cable data from the Valhall field — Part 1: Imaging compressional wave speed, density and attenuation: *Geophysical Journal International*, **194**, 1640–1664, doi: [10.1093/gji/ggt177](https://doi.org/10.1093/gji/ggt177).
- Quan, Y., and J. M. Harris, 1997, Seismic attenuation tomography using the frequency shift method: *Geophysics*, **62**, 895–905, doi: [10.1190/1.1444197](https://doi.org/10.1190/1.1444197).
- Reine, C., R. Clark, and M. van der Baan, 2012, Robust prestack *Q*-determination using surface seismic data — Part 1: Method and synthetic examples: *Geophysics*, **77**, no. 1, R45–R56, doi: [10.1190/geo2011-0073.1](https://doi.org/10.1190/geo2011-0073.1).
- Sams, M., and D. Goldberg, 1990, The validity of *Q* estimates from borehole data using spectral ratios: *Geophysics*, **55**, 97–101, doi: [10.1190/1.1442776](https://doi.org/10.1190/1.1442776).
- Shekar, B., and I. Tsavkin, 2011, Estimation of shear-wave interval attenuation from mode-converted data: *Geophysics*, **76**, no. 6, D11–D19, doi: [10.1190/geo2010-0415.1](https://doi.org/10.1190/geo2010-0415.1).
- Shekar, B., and I. Tsavkin, 2014, Kirchhoff modeling for attenuative anisotropic media using Gaussian beams: *Geophysics*, **79**, no. 5, WB51–WB61, doi: [10.1190/geo2013-0432.1](https://doi.org/10.1190/geo2013-0432.1).
- Tarantola, A., 1984, Inversion of seismic reflection data in the acoustic approximation: *Geophysics*, **49**, 1259–1266, doi: [10.1190/1.1441754](https://doi.org/10.1190/1.1441754).
- Tarantola, A., 1988, Theoretical background for the inversion of seismic waveforms including elasticity and attenuation: *Pure and Applied Geophysics*, **128**, 365–399, doi: [10.1007/BF01772605](https://doi.org/10.1007/BF01772605).
- Tiwari, U. K., and G. A. McMechan, 2007, Effects of incomplete parameterization on full-wavefield viscoelastic seismic data for petrophysical reservoir properties: *Geophysics*, **72**, no. 3, O9–O17, doi: [10.1190/1.2716631](https://doi.org/10.1190/1.2716631).
- Tromp, J., C. Tape, and Q. Liu, 2005, Seismic tomography, adjoint methods, time reversal and banana-doughnut kernels: *Geophysical Journal International*, **160**, 195–216, doi: [10.1111/gji.2005.160.issue-1](https://doi.org/10.1111/gji.2005.160.issue-1).
- Tsvavkin, I., and V. Grechka, 2011, Seismology of azimuthally anisotropic media and seismic fracture characterization: SEG.

- Virieux, J., S. Operto, H. Ben-Hadj-Ali, R. Brossier, V. Etienne, F. Sourbier, L. Giraud, and A. Haidar, 2009, Seismic wave modeling for seismic imaging: The Leading Edge, **28**, 538–544, doi: [10.1190/1.3124928](https://doi.org/10.1190/1.3124928).
- Xue, Z., T. Zhu, S. Fomel, and J. Sun, 2016, Q -compensated full-waveform inversion using constant- Q wave equation: 86th Annual International Meeting, SEG, Expanded Abstracts, 1063–1068.
- Zhu, T., J. M. Carcione, and J. M. Harris, 2013, Approximating constant- Q seismic propagation in the time domain: Geophysical Prospecting, **61**, 931–940, doi: [10.1111/gpr.2013.61.issue-5](https://doi.org/10.1111/gpr.2013.61.issue-5).
- Zhu, T., J. M. Harris, and B. Biondi, 2014, Q -compensated reverse-time migration: Geophysics, **79**, no. 3, S77–S87, doi: [10.1190/geo2013-0344.1](https://doi.org/10.1190/geo2013-0344.1).
- Zhu, Y., and I. Tsvankin, 2006, Plane-wave propagation in attenuative transversely isotropic media: Geophysics, **71**, no. 2, T17–T30, doi: [10.1190/1.2187792](https://doi.org/10.1190/1.2187792).
- Zhu, Y., I. Tsvankin, P. Dewangan, and K. van Wijk, 2006, Physical modeling and analysis of P-wave attenuation anisotropy in transversely isotropic media: Geophysics, **72**, no. 1, D1–D7, doi: [10.1190/1.2374797](https://doi.org/10.1190/1.2374797).